Applied Surface Science 576 (2022) 151822

Contents lists available at ScienceDirect

Applied Surface Science

journal homepage: www.elsevier.com/locate/apsusc

Full Length Article

Electrodeposited CuO thin film for wide linear range photoelectrochemical glucose sensing

Neville J. Cory [a], Eran Visser [a], Jessica Chamier [b], Juliet Sackey [c], Franscious Cummings [d], Mahabubur Chowdhury [a,*]

[a] Department of Chemical Engineering, Cape Peninsula University of Technology, Bellville 7535, South Africa
[b] Department of Chemical Engineering, Centre for Catalysis Research, HySA Catalysis, University of Cape Town, Cape Town 7700, South Africa
[c] Nanosciences African Network (NANOAFNET), iThemba LABS-National Research Foundation, Old Faure Road, 7129 Somerset West, South Africa
[d] Electron Microscope Unit, University of The Western Cape, Bellville 7535, South Africa

ARTICLE INFO

Keywords:
Thin Film
CuO
Photoelectrochemical
Glucose sensor
Band gap tuning
Etching

ABSTRACT

Cupric oxide (CuO) has been used as a non-enzymatic glucose sensor for decades. However, there is a paucity of publications on bare CuO-based photo electrochemical (PEC) glucose detection. In this study, a photo active CuO thin film was electrodeposited onto conductive glass and its band gap was tuned by etching in NH_3 solution. A 6 W light-emitting diode (LED) bulb was used as the light source for PEC glucose oxidation. Various physical and electrochemical characterization techniques were used to study the PEC behavior of the CuO thin film electrode during glucose oxidation. The electrochemical oxidation of glucose was found to be an irreversible electron transfer process controlled by diffusion at the electrode surface under illumination and dark conditions. Electrochemical impedance spectroscopy (EIS) confirmed that the charge transfer resistance in the light decreases by several orders of magnitude. Good amperometric performance was obtained for the CuO film with a 4 s response time and negligible interference from other species present in human blood. The as prepared sensor exhibited a remarkable wide linear range up-to 29 mM.

1. Introduction

Diabetes has been affecting the human population for over three millennia. This disease is characterized by irregular glucose levels in the blood. The human body detects these irregularities and subsequently releases the hormone, insulin which is responsible for the removal of glucose from the bloodstream by converting glucose into glycogen. Our body's inability to make effective use of or produce insulin is termed diabetes. Several studies have revealed that glucose level monitoring and controlling, both increased the life expectancy of patients living with the disease as well as reduced the co-morbidities associated with it [1,2]. Transition and precious metals have shown great promise toward glucose detection, however, their high costs have hindered their application for a real world solution [3]. A need for more cost-effective non-enzymatic glucose detection, has steered research toward the development and inclusion of metal oxides (MO's) such as Co_3O_4, CuO, NiO, TiO_2, Cu_2O and ZnO in glucose sensors [4,5].

Photo-activated electrochemical (PEC) sensors based on photocatalytic systems have lately been used for electroanalytical purposes, i.e., glucose detection, and they have attracted a lot of interest because of their high sensitivity and minimal background noise. Photoactive materials with excellent optoelectronic capabilities are essential for building the PEC sensor. MO semiconductors are mostly used in conjunction with a conductive support material, which shuttle electrons to promote conductivity. The majority of these systems are based on TiO_2, a semiconductor material that has gotten a lot of interest for applications like gas sensors, solar cells, and water sensors [6]. Most of the MO based non-enzymatic glucose sensors suffer from a low linear range. This hinders the role out of MO based non-enzymatic glucose sensors for real life applications.

Recently Cu_2O was used as a PEC sensor for glucose [7]. Vertical nanowires of CuO has been used a PEC biosensor for ethanol detection [8]. Even though glucose sensing is critical, research regarding pristine CuO electrodes for electrochemical glucose sensing is surprisingly restricted. Comparatively, tenorite (CuO) enjoys the narrowest band gap thus requires less photon energy incident on its surface to produce a photocurrent. CuO has been considered as a potential game changer with its impressive sensing performance over the years.

* Corresponding author.
E-mail address: chowdhurym@cput.ac.za (M. Chowdhury).

https://doi.org/10.1016/j.apsusc.2021.151822
Received 13 August 2021; Received in revised form 2 October 2021; Accepted 4 November 2021
Available online 9 November 2021

Deposition or attachment of MO films onto substrates often requires costly or time-consuming techniques such as vapor deposition, hydrothermal synthesis or spin coating. Alternatively, electro-deposition is a highly scalable technique that allows for rapid synthesis of nanomaterials while displaying high porosity and increased surface area [9]. In addition, this technique allows for a highly reproducible nanostructure further aiding in up-scaled production. A post electrodeposition treatment such as etching has in the past been found to enhance the electronic characteristics of copper oxides and even reshape their surfaces [10,11].

In this study a CuO thin film was electrodeposited onto conductive glass for PEC detection of glucose over an ultrawide range (up to 29 mM) using a very low powered LED light (6 W). The PEC sensor also showed good inter and intra electrode reproducibility and a fast response time of 4 s.

2. Experimental methods

2.1. Materials

Copper Cyanide (CuCN), Sodium Cyanide (NaCN), Sodium Carbonate (Na_2CO_3), d-(+)-Glucose, Ascorbic Acid (AA), Sodium Hydroxide (NaOH), Fructose, Sucrose, Sodium Chloride (NaCl), Uric Acid (UA), Citric Acid (CA), Acetaminophen and Fluorine doped Tin Oxide (FTO) glass were purchased from Sigma Aldrich South Africa and used without any further purification.

2.2. CuO thin film electrode synthesis

The CuO photocatalyst thin film deposition involved the optimization of three separate processes, i.e. electro-deposition, calcination and etching. The results pertaining to the "as-deposited" and "calcined" samples are included in the supplementary document unless stated otherwise. The Fluorine doped Tin Oxide (FTO) glass sheet was cut into 4 × 1.5 cm slides. These slides along with all glassware and stirring beads were ultrasonically cleaned with degreaser for 15 min, followed by a mixture of ethanol and acetone for another 15 mins and finally sonicated in deionized water. The glassware and slides were dried in a convection oven at 60 °C for 4 h. Electro-deposition of a CuO layer from a cyanide strike solution containing 0.036 M CuCN, 0.067 M NaCN and 0.014 M Na_2CO_3 was carried out at 4 V for 2 min. The anode and cathode used were both cleaned FTO glass slides submerged 2 cm into the solution and separated by a constant distance of 4 cm. The FTO slides with the electrodeposited layer were annealed in a furnace for 1 h at 450 °C at atmospheric pressure. After allowing the samples to cool to room temperature, they were submerged into vials containing sufficient NH_3 at 25% (V/V) for 2 min. An overview of the synthesis procedure is presented in Fig. 1a. The overall synthesis process involved the optimization of the three-separate process (Electrodeposition, Calcination and Etching). The deposition voltages investigated were 2 V, 3 V, 4 V and 5 V over a time (min) of 0.5, 1, 2 and 4 respectively. The calcination temperatures were varied from 100, 250, 350, 450, 550 and 650 °C for 1, 2, 3 and 4 h respectively. The NH_3 concentration was kept constant

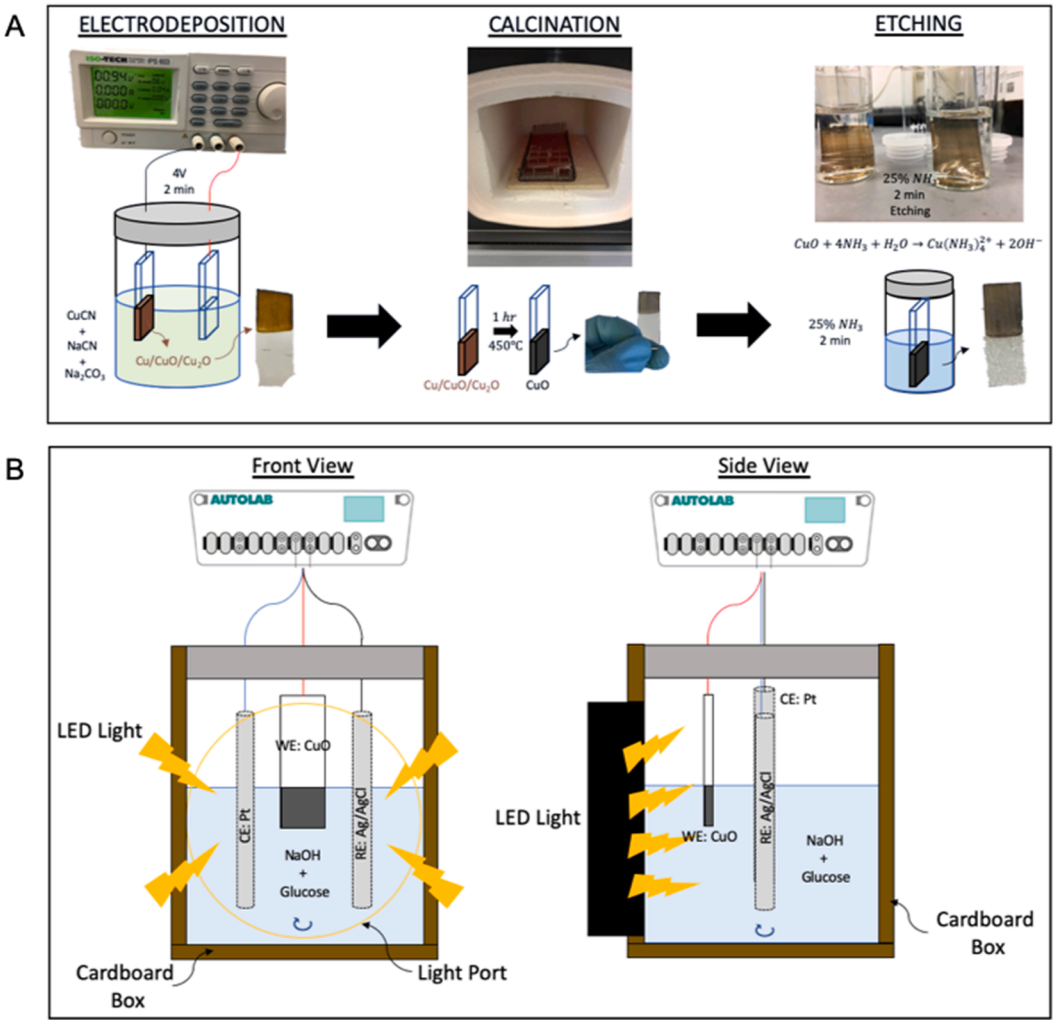

Fig. 1. Schematics of the A) thin film CuO electrode fabrication and B) PEC testing procedure.

however the submersed times were varied between 1, 2 and 4 mins. Each synthesis stage was optimized by identifying the maximum difference between the anodic peak currents in the light and dark conditions to achieve enhanced photo-electrochemical glucose detection.

2.3. Electrochemical characterization

The electrochemical experiments were conducted using a three-electrode set-up and Autolab PGSTAT302 N potentiostat. The CuO thin film was used as the working electrode, an Ag/AgCl (3 M KCL) reference electrode and a platinum wire counter electrode. All testing solutions were 0.1 M NaOH containing glucose at designated concentrations for cyclic voltammetry and chronoamperometry evaluations. The cyclic voltammograms (CV's) conducted in the dark were performed in an optical (quartz) glass box with dimensions of $5 \times 5 \times 5$ cm^3 and a 2 mm thick wall housed in cardboard to block ambient light. The same cardboard housing was used for samples undergoing illumination through a cut out in the box just big enough to fit the light source as shown in Fig. 1b. The light source was a cool white LED (6 W, 540 lm) with accompanying LED driver powered by NOVA 2.0 software. The potential window for the CV's ranged from 0.0 V to 0.8 V vs Ag/AgCl over 25, 50, 100 and 200 mV/s scan rates. Electrochemical impedance spectroscopy (EIS) experiments were conducted in 0.1 M NaOH solution with and without glucose in the light and dark over a frequency range of 0.1 Hz to 10^5 Hz with and applied 5 mV AC bias. All electrochemically tested samples surfaces were limited to only 1 cm^2 exposure using lacomit varnish.

2.4. Surface characterization

Phase identification was done using x-ray diffraction (XRD). The "etched" samples were characterized using a Cu- $K\alpha$ radiation source at an operational tube voltage of 45 kV and a current of 40 mA. The diffraction patterns were collected at increments of 0.02 via a continuous scan. All X-ray photoelectron spectroscopy (XPS) measurements were conducted using a Thermo-ESCAlab 250Xi with a monochromatic Al- $K\alpha$ source (1486.7 eV) and a power of 300 W at an operational pressure of 10^{-8} mBar. A Zeiss Auriga field emission scanning electron microscope (SEM) was employed to evaluate the morphology and to determine the layer thickness for Hall Effect measurements. All images were collected using an in-lens secondary electron detector with the beam accelerated to an accelerating voltage of 5 kV. The Hall Effect measurements were conducted at 300 K, 500 μA and 0.55 T using an Ecopia HMS-3000 measuring system. The optical properties of the samples were conducted on a Cary 5000 UV–Vis-NIR spectrophotometer equipped with an integrating sphere within wavelength range of 200–2500 nm.

3. Results and discussion

3.1. Thin film electrode surface characterization

An analysis of Fig. 2a revealed the "calcined" sample was comprised of structural features indicative of a monoclinic structure indexed from PDF-01–070-6831 [12]. The findings confirmed that a CuO film was synthesized and no peaks were recorded for any other Cu species. The was no evidence of peak broadening or peak shifts between the "calcinated" and "etched" samples. The stability of the diffractograms suggested that the crystallographic CuO structure remained monoclinic even after NH_3 etching. Major amplitude decreases were recorded for most FTO peaks. Similarly, the intensity of the CuO peaks remained mostly unchanged up to a scan angle of $2\theta = 50$. Extending the scan angle past this point revealed that the $(20\bar{2})$, $(11\bar{3})$, $(22\bar{1})$, $(31\bar{2})$, $(13\bar{2})$, and $(20\bar{4})$ intensity decreased by approximately a third though no shift or peak broadening were observed. This decrease in intensity may be associated with thinning of the CuO layer as would be expected via etching as is further analyzed using SEM.

SEM images presented in Fig. 2B show morphological transitions between the calcined and etched stages. Post calcination Fig. 2B (1.1–1.2), the particles appear to fuse together in trapezoidal shapes with regular grain sizes and crystallinity. The "as-deposited" sample SEM images haves been included in the supplementary as Fig. S1. Upon etching the surface of the calcined thin films Fig. 2B (2.1–2.2), the trapezoidal nanostructures size reduced, which may have increased the surface area of the thin film. This decrease in film thickness confirmed the removal of a thin layer of CuO from the surface of the electrode and the decrease in peak intensity presented on the XRD diffractograms. The film was at its thickest ($\approx 225nm$) after calcination and reduced by a 12 % ($\approx 200nm$) following etching.

The core Cu 2p, O 1 s, C 1 s and Sn 3d peaks are presented in the XPS plots shown in Fig. 3. The Cu 2p core level's emission spectra for the "etched" sample feature two peaks corresponding to Cu $2p_{3/2}$ and Cu $2p_{1/2}$ at binding energies of 933.4 eV and 953.2 eV respectively. The former binding energy is assigned to Cu^{2+} ions which is characteristic of the CuO phase while the latter further confirms the presence of CuO by matching with the standard XPS spectra for CuO [13]. At least three satellite peaks are recorded at higher binding energies relative to their main peaks at 940.8 eV, 943.4 eV and 962.0 eV which are assigned to the Cu $3d^9$ configuration. The position of the Cu $2p_{3/2}$ peak with respect to its satellite indicates the existence of two CuO configurations which are the Cu $3d^{10}$ and the Cu $3d^9$ (ground state) [14]. This further confirmed the presence of CuO. The binding energies associated with the O 1 s XPS spectra revealed a strong peak at 529.2 eV which is associated with a metal–oxygen bond in the lattice. A peak at 529.4 eV confirms the M—O

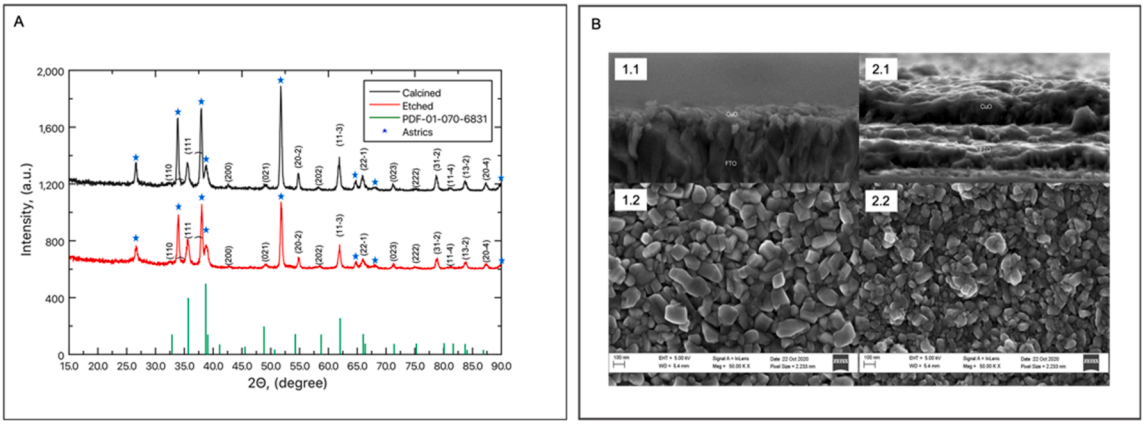

Fig. 2. Surface characterization of etched CuO thin film electrode; A) XRD and B) Cross sectional and surface SEM images respectively for Calcined (1.1–1.2) and Etched (2.1–2.2) electrode.

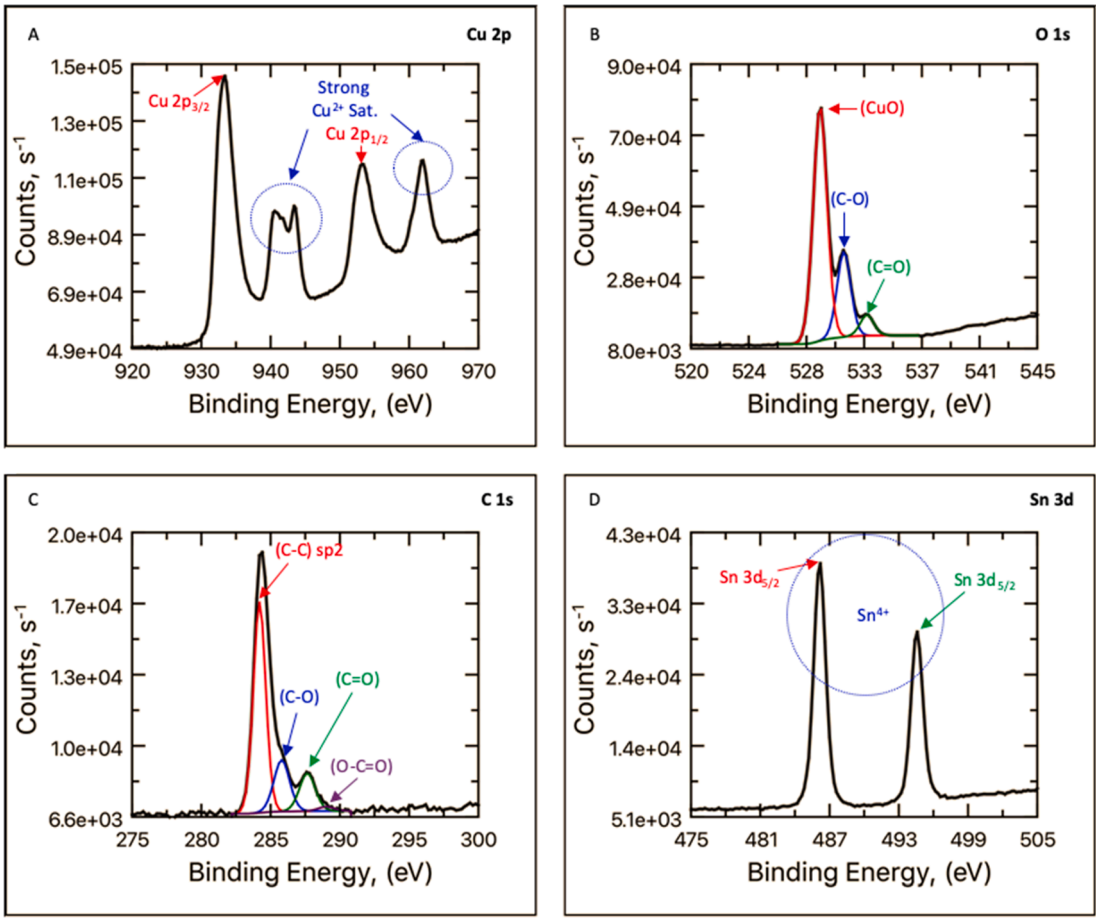

Fig. 3. XPS spectrographs for the "etched" sample measured for A) Cu 2p, B) O 1 s, C) C 1 s, and D) Sn 3d.

bond is in fact a Cu—O bond, however, some impurities were detected in the form of C—O bond at 531.0 eV and a C═O bond at 532.8 eV. The detection of these impurities is common in samples which have been stored in air as opposed to an evacuated vial. XPS did not detect any form of (—OH) species on the samples surface though the carbon-based impurities were further investigated in the C 1 s core level scan. A sp^2 (C—C) peak was detected at 284.2 eV along with a secondary confirmation of the contaminant (C—O) and (C═O) species at 285.8 eV and 287.6 eV respectively. Finally, it was confirmed that the FTO glass substrate remained un-altered after etching in NH_3 as Sn^{4+} was detected.

Raman spectroscopy was employed to characterize the molecular states in selected samples. The Raman peaks presented in Fig. 4 occur at 280.6, 323.3 and 613.4 cm^{-1} respectively.

The results revealed three common peaks for the various synthesis stages which confirmed that the primary molecular state remained stable. The primitive cell of CuO contains two molecules such that there exists nine optical zone-centered modes, namely $A_g + 4A_u + 2B_g + 5B_u$ [15]. Of these, only three modes are Raman active ($A_g + 2B_g$). Upon comparison with other works, the 280.6 cm^{-1} peak can be assigned to the A_g whilst the 323.3 cm^{-1} and 613.4 cm^{-1} are B_g modes [16]. The intensities of the peaks have been normalized however; it can be noted that the intensity of the "as deposited" sample after 50-cycles is much sharper as compared to the others. It has been reported that intensity is related to grain size and that Raman peaks are observed to shift with grain size variations [17]. Considering the SEM images showed an apparent increase in surface area; the small deviations noted among the wave numbers in the Raman spectra are attributed to the grain size differences, post etching. Raman can also be used to identify the presence of unintended species such as Cu_2O or even $Cu(OH)_2$ [18]. Glucose has been reported to reduce copper hydroxides to form cupric oxide

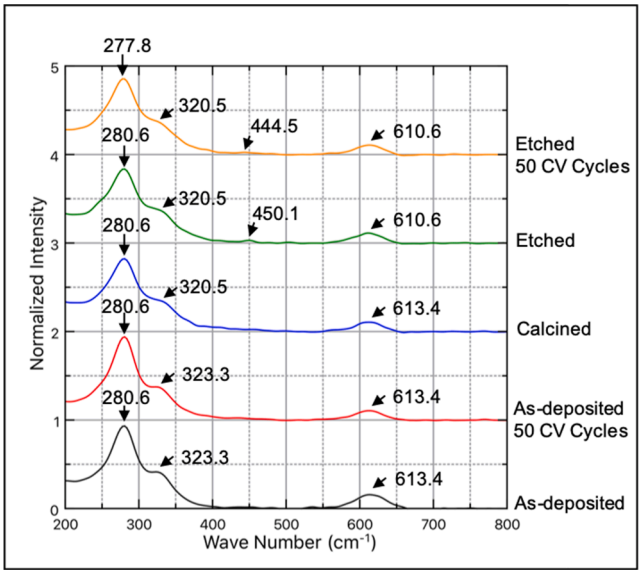

Fig. 4. Raman spectra for the various stages of synthesis including those following 50 CV cycles.

according to Equation (1), [19], however the Raman data obtained for samples after glucose testing shows no Cu_2O in any of the films.

$$Cu(OH)_2 + C_6H_{12}O_6 \rightarrow Cu_2O + H_2O \quad (1)$$

New minor peaks form after etching at 450.1 cm^{-1} and decreases to

444.5 cm^{-1} following glucose testing. Based on the position and lack of intensity of these peaks, it is plausible that a small amount of surface hydroxyl species was introduced onto the film post-etching. Surface hydroxyl species will not be detected in XPS as the analysis is performed under vacuum and will likely cause any trace hydroxyls to fall to oxide. Also, XRD will not show surface hydroxyls as these species are non-crystalline. The presence of such a small amount of surface hydroxyl is believed to not make any active contribution toward glucose sensing nor its properties. Following thermal oxidation, the 323.3 cm^{-1} peak decreases to 320.5 cm^{-1} which may be as a result of the increased presence of oxygen in the crystal structure as seen in the XPS data. Then post-etching, the 613.4 peak shifts to 610.6 cm^{-1} and is ascribed to the decrease in crystallinity in the A_g mode.

3.2. Electronic properties of the CuO thin film electrode

To better understand the electronic transport of the deposited semiconductor, Hall Effect measurements were performed to identify the type of charge carriers, the carrier concentration, Hall mobility as well as conductivity of the samples. These parameters are included in the supplementary Table S1 for the "As-deposited", "Calcined" and "Etched" samples including tests conducted after 50 CV cycles. The thicknesses of the films were obtained from SEM images and reported alongside the Hall measurements. From the Hall coefficients it can be deduced that throughout the synthesis and testing process, the CuO film remains an n-type semiconductor. This is due to the negative relation of the Hall coefficients, which decrease through the stages of fabrication. In addition, these findings reveal that the majority charge carriers are electrons. This means that although no doping occurred for these samples, there exists a donor state close to the conduction band which can accept free electrons within the band gap. This n-type behaviour is due to oxygen vacancies commonly found in nanostructured metal-oxides. The Van der Pauw method was applied in an iterative process to determine the charge carrier mobility and sheet concentration. The carrier mobility tripled (7.91 → 25.4 cm^2/Vs) following the "calcination" step which is due to the increased crystallinity and uniform morphology along with the increase in layer thickness seen in the SEM images. Additionally, the grain sizes were larger in the calcined sample and are inclination free which could result in a more direct flow path. A decrease in mobility was found following the etching stage due to the decreased particle sizes, uniformity and layer thickness. The etched samples mobility (12.3 cm^2/Vs), however, is close to double that of the original as deposited sample (7.91 cm^2/Vs). A three-fold increase in resistivity (5.89E-5 → 1.94E-4 Ωcm) yielded an approximately equivalent threefold increase in carrier mobility. Wu and co-authors (2014) noted that high resistivities (better insulators) are associated with low carrier mobilities though are greatly influenced by temperature. This could be the reason for the abnormally decreased resistivity and mobility seen in the etched sample data [20]. The calculated resistivities in this work are very low and more comparable with that of bulk Cu. Nevertheless, there are reports where the resistivities of CuO-based nanomaterials fall between 2.0E +5 and 1.0E + 6 Ωcm [21–23]. During electrodeposition, the formation of electrically active vacancies could be replaced by neutral CuO sites which lead to decreased resistivities and so upon calcination, an increase in the generation of carriers in the crystalline structure [24] occurs. Low range resistivities especially for semiconductors are highly sought after as it shows better conductivity which translates to increased mobility. The bulk carrier concentration (−8.85E + 20 cm^{-3}) was the largest in the etched sample which could explain why it showed relatively high mobilities. Other authors have noted carrier concentrations of 4.0E + 18, 9.0E + 19 and 6E + 20 cm^{-3}, of which some are several orders of magnitude smaller than those presented in this work [20,22,25]. Such high charge carrier concentrations could be an indication of low valence band maximums which cause fermi-level pinning [26]. Li et al. investigated the relationship between carrier concentration and mobility while comparing the effects to sensing performance. They found that decreased carrier concentrations and increased carrier mobilities resulted in higher sensitivity [27].

3.3. Optical properties of the CuO thin film electrode

The UV–Vis diffuse reflectance spectra of the "As-deposited", "Calcined" and "etched" CuO samples were assessed to determine the light absorption properties of these films. The spectra were run from a wavelength of 200 nm to 2500 nm while recording the reflectance R (%). The optical band gap of semiconductors can be evaluated using the theory from Kubelka and Munk [28]. As the Tauc method assumes the absorption coefficient (K) is energy dependent, it may be replaced with a ratio of (K) and the scattering coefficient (S). Fig. S2 A, shows the reflectance spectra for the three samples and while Fig. S2 B reveals the absorption (K) and scattering coefficients (S) in relation to the photon energy. From the reflectance spectra, the ratio (K/S) was determined by applying the following relationship.

$$F(R_\infty) = \frac{K}{S} = \frac{(1 - R_\infty)^2}{2R_\infty} \tag{2}$$

where $R_\infty = \left(R_{Sample}/R_{Stardard}\right)$ represents the reflectance of a sample with infinite thickness, K denotes the absorption coefficient whilst S is the scattering coefficient. Upon substitution of this ratio into the modified Tauc relation, the following equation is obtained.

$$\left(\frac{K}{S}(h\upsilon)\right)^n = B(h\upsilon - E_g) \tag{3}$$

Here, $h\upsilon$ is the photon energy, B is a constant and E_g is the band gap. The n power is especially important as this defines the nature of the electron transition which is associated with direct or indirect bands. When $n = 0.5$, a "direct allowed" band structure is present and if $n = 2$, an "indirect allowed" band structure prevails. However, n can also be 2/3 in which case the transition is "direct forbidden" and also 1/3 for "indirect forbidden" [29]. Based on these variations to the model, the optical band gap can change dramatically depending on the value of n. Typically, the transition for CuO exhibits a direct band (DB) structure though some reports indicate indirect band (IB) gaps [30]. The band gap of a semiconductor is determined by identifying the type of transition via examining the position of the absorption edge. Diffuse Reflectance Spectroscopy (DRS) measurements offer identification of the absorption coefficient which is used in the modified Tauc relation (Eq. (3)). A straight line is drawn through the steep region where the absorption increases with hυ. The band gap approximations for the samples were determined using the x-axis ($h\upsilon$) intercepts of the plots in Fig. 5. Following DB transitions, (E_g) decreased accordingly; "As Deposited" > "Calcined" > "Etched". Lee and Wang (2021) determined that annealing temperatures above 400 °C led to single CuO phase formation whilst reducing the E_g by as much as 0.56 eV as compared to its as-deposited counterpart [31]. An E_g of 1.19 eV was found for the etched sample, 1.40 eV for the calcined sample and the As-Deposited sample displayed the largest optical band gap of 1.59 eV under DB transitions. The E_g decrease between the As-deposited and calcined samples is believed to be as a result of the increased crystallinity post-annealing accompanied by the fusion of smaller crystals into larger ones. In contrast, the IB transition in Fig. 5B reveals a large increase in band gap energy post calcination. Two band gaps were identified for the As-deposited sample at 2.00 eV and 2.17 eV while for the Calcined and Etched samples the band gaps were found to be 3.66 eV and 3.49 eV, far outside those typically reported for CuO (1.2–2.1 eV). Based on these findings combined with the elucidations from XRD, XPS and Raman, we believe that the CuO film synthesized undergoes direct band transitions.

Quantitatively, it is also observed that in both DB and IB transitions, the band gap decreases post NH_3 etching. This is believed to be as a result of a decrease in the optical reflection between the calcined and

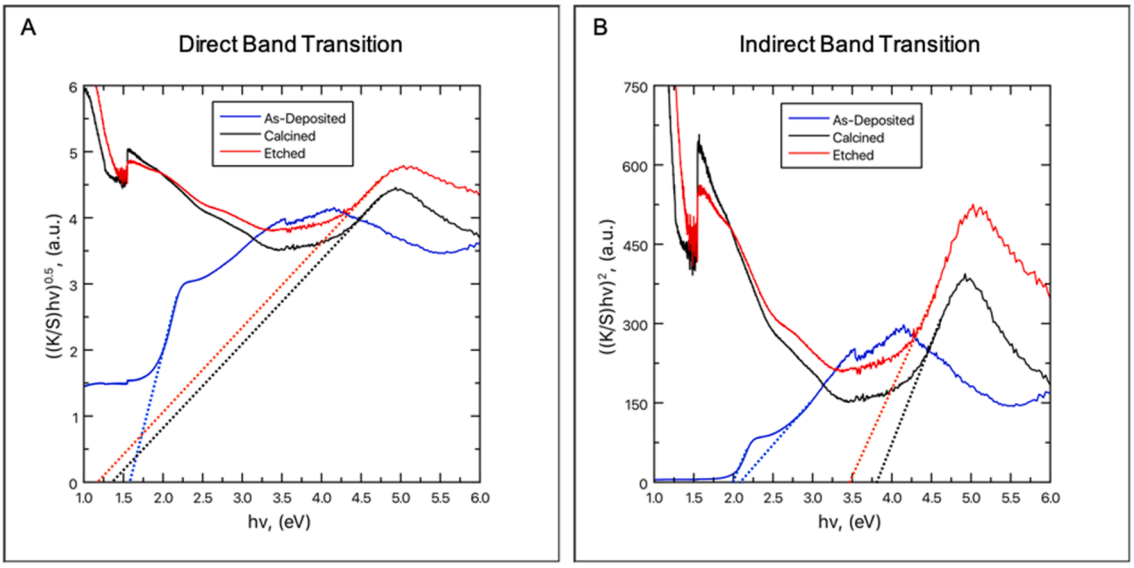

Fig. 5. Band gap determination via A) Direct band transition at n = 0.5 and B) Indirect band transition with n = 2.

etched samples at shorter wavelengths. It can be seen from the SEM images that the surface of the film presents more concave arrangements resulting in a more textured surface post-etching and could result in decreased reflection via increased scattering [11]. This also agrees well with the anti-reflective properties of silicon nanotips and GaSb nanopillar arrays which showed decreased reflection upon etching [32]. Minimizing the loss of light energy due to reflection coupled with less film transparency via a rougher surface leads to enhanced absorption thereby decreasing the optical band gap.

3.4. Photoelectrochemical behavior

The electrochemical characterization of the CuO film was evaluated using cyclic voltammetry (CV) in an alkaline medium (0.1 M NaOH) both in the presence and absence of glucose with and without illumination. Glucose is non-conductive as it dissolves in water but does not dissociate. In an effort to counter this, NaOH bridges the gap and allows for a conductive solution. Human blood also slightly basic with a pH of approximately 7.4, thus incorporation of NaOH during testing is a commonly accepted practice [33]. The electrochemical activity towards the oxidation of glucose was measured in a 1 mM solution of glucose in the dark and light through the optical box. A total of 10 stabilization cycles were performed before the data was recorded to ensure stability. Using the optimized synthesis parameters (4 V for 2 mins electrodeposition, 450 °C calcination for 1 h and 2 mins of NH_3 etching) the resultant current densities are represented in Fig. S3. The current density of the "as-deposited" CuO film is the greatest at 1.87 mA/cm^2 in the dark. In the light however, the current increases by only 0.175 mA/cm^2. The "as-deposited" CuO film produced the smallest difference between dark and light, its photoactivity toward glucose was inferior when compared to the calcined and etched samples. This may be due to its increased band gap (1.59 eV) compared to the calcined samples. Nevertheless, the current density produced by this sample in the presence of 1 mM glucose was impressive as it enjoys higher current densities in both light and dark scenarios. The increase in current density for the calcined samples was 0.261 mA/cm^2 whilst the greatest difference was recorded for the etched sample with an increase of 0.328 mA/cm^2 from dark to light. A possible reason for this increase in photocurrent could again be attributed to the decrease in band gap from calcined (1.40 eV) to etched sample (1.19 eV). A smaller band gap in a semiconductor translates to less energy being required to promote an electron from the valence band into the conduction band. This clearly shows that the inclusion of the etching stage enhanced the CuO band gap, charge transfer properties as well as the difference in light/dark peak current. The oxidation of carbohydrate species on Cu-based electrodes occurs over a similar potential range to that of the Cu (III) species formation. The redox couple between Cu(II)/Cu(III) is reported to occur at potentials 0.58 and 0.61 V vs Ag/AgCl in 0.1 M NaOH [34]. Non-enzymatic glucose electrooxidation is believed to be mediated by this redox couple as CV measurements indicate oxidation over this wide potential range. The formation of the Cu_2O_3 species has also been reported, however under the same alkaline conditions (0.1 M NaOH) this formation occurs at higher potentials than oxygen evolution [35]. The formation of highly reactive hydroxide radicals has been proposed to act as the mediators in glucose oxidation. The standard potential for this redox pair (E greater than 1.33 V) is, however, well outside the potential window tested [36]. The glucose oxidation mechanism therefore most often considered by other researchers involves the formation of highly oxidative Cu^{3+} species. This demands the formation of individual, or a combination of, Cu^{3+}, CuO_2^-, Cu_2O_3, CuOOH, $Cu(OH)_3$ or $Cu(OH)_4$ species for the process to proceed [35,37]. The reactions associated with Cu(II)/Cu(III) redox pair are summarized in Equations 4–6 and glucose is oxidized as per Equation (7) to form gluconic acid after hydrolysis of gluconolactone:

$$CuO + OH^- + H_2O \rightarrow Cu(OH)_3 + e^- \quad (4)$$

$$CuO + 2OH^- + H_2O \rightarrow Cu(OH)_4 + e^- \quad (5)$$

$$CuO + OH^- \rightarrow CuOOH + e^- \quad (6)$$

$$Cu^{3+} + Glucose \rightarrow Cu^{2+} + Gluconolactone \quad (7)$$

Barragan et al (2018) determined that while the CuOOH species is most commonly used to describe the glucose oxidation mechanism via Cu^{3+}, no equilibrium potential nor CV peaks are obtained for its reaction [2]. Although it is well known that CuO exhibits semiconductive behaviour, few works make use of this property and information regarding the photo-electrochemical oxidation of glucose is scarce. These photoelectro-oxidative properties of CuO were investigated under cool white LED illumination (6 W, 540 lm) in a blank 0.1 M solution of NaOH and 1 mM glucose solution. As per the CVs in Fig. 6A, in the absence of glucose at 100 mVs^{-1} scan rate, there are no observable redox peaks for both bare FTO nor for the etched CuO electrode. A prominent current plateau is evident in both cases with an exponential anodic current increase at potentials greater than 0.65 V for this CuO electrode.

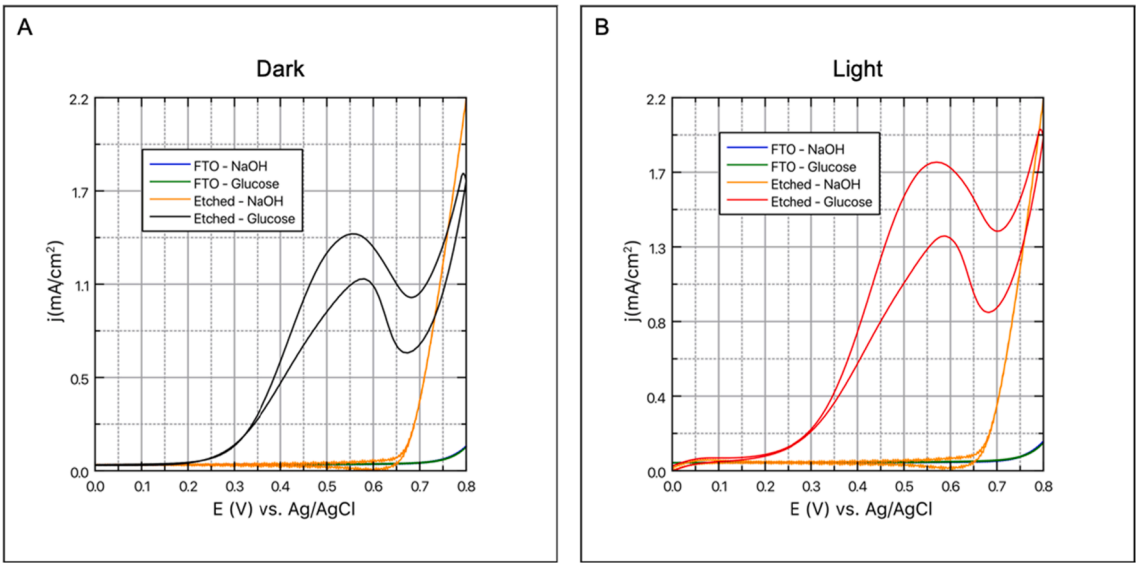

Fig. 6. Electrochemical behavior at 100mVs^{-1} scan rate for the etched CuO electrode in a blank NaOH and 1 mM glucose solution under A) dark and B) light, conditions.

This rapid current rise can be attributed to the formation of oxygen on the surface of the electrodes following the oxidation of OH^- ions [2,38,39].

The separation observed between the forward and reverse scan of the etched sample in 0.1 M NaOH could be attributed to the chemical reaction Eq. 8–9 [40].

$$Cu(OH)_2 + OH^- \rightarrow CuOOH + H_2O + e^- \quad (8)$$

$$CuO + OH^- \rightarrow CuOOH^- + e^- \quad (9)$$

The shape of the CV curve presented in Fig. 6 changes dramatically with clear oxidation peaks evident in the presence of glucose both in the dark and light. This isolates the electrocatalytic activity toward glucose as being solely due to the copper species deposited on the substrate. Fig. 6A features an oxidation peak at 0.56 V vs Ag/AgCl accompanied by an anodic current density of 1.41 mA/cm^2. These peaks occur well above the current plateau observed in the blank solution. Fig. 6B shows CV-curves, in which the significant enhancement of the oxidation process by light-illumination is readily observed. The etched CuO electrode presents anodic photocurrents in the presence of glucose in the dark and light at onset potentials of 0.27 V and 0.15 V respectively. A decrease in onset potential has previously been reported, however, it is very unique for Cu based electrodes [41]. A peak current density of 1.795 mA/cm^2 was observed while illuminated, which, equates to an increase of 0.382 mA/cm^2, far greater than in the dark. Although the general CV shape appears consistent, upon closer examination it was found that under illumination, the oxidation potential increased by 0.014 V thus requiring an applied potential of 0.576 V. This small potential change is attested to a shift in the equilibrium position of the system to less anodic values.

Due to the semiconductive nature of CuO and the subsequent increase in current density as seen by the voltammograms in the light, it is required to investigate alternate mechanisms which could explain this increase. An overall depiction of the possible reaction pathways for the oxidation of glucose in both the light and dark is represented in Fig. 7A. Both reaction pathways 1 and 2 have been well documented for group (III) M—O for glucose oxidation in the dark [2,41–43]. The etched CuO film was excited by the light incident on its surface resulting in the generation of e^- and h^+ which undergo charge separation as depicted in pathway 3. The conduction band (CB) energy level for FTO is lower than that of CuO which results in electron transfer from CuO to FTO as this is the more energetically favorable process [44]. Good contact between the FTO and CuO due to the high calcination temperature provided the ideal electron transport system which translated into high light sensitivity and aided in reducing electron hole pair recombination. The CuO(h^+) left behind in the valence band (VB), pair with OH^- ions which are oxidized to form hydroxyl radicals under the assumption that charge transfer occurs efficiently [2]. These radicals desorb from the CuO surface and so leave behind an active site for more hydroxyl ions to adsorb to [45]. Glucose molecules are then attacked by the radicals as depicted in Fig. 7B. The radicals react with D-glucose by means of hydrogen abstraction that forms an intermediate glucose species with a carbon centered radical. This is followed by oxygenation of the subsequent intermediate by releasing a carbonyl group which forms gluconolactone

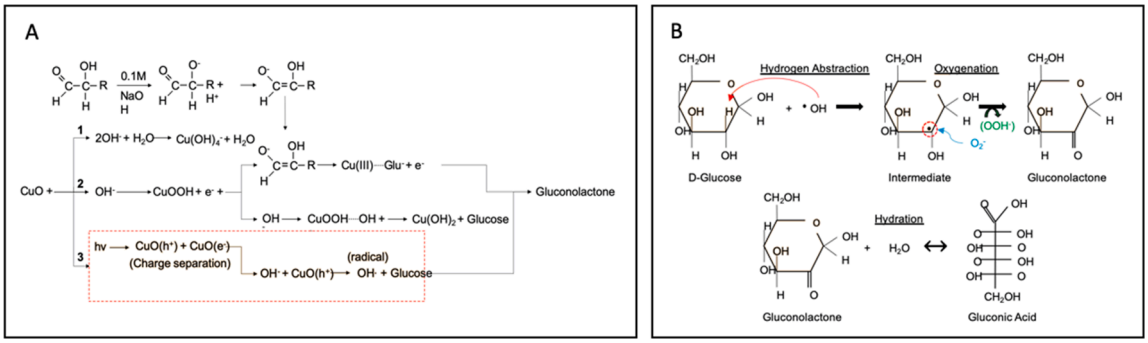

Fig. 7. Possible glucose oxidation mechanism, A) various oxidation pathways and B) hydroxyl radical mediated glucose oxidation.

[46]. Hydration of the gluconolactone species results in the reversible gluconic-acid/gluconolactone system.

The glucose sensing mechanism during illumination is represented in pathway 3 (Fig. 7A) and aligns well with other reports of carbohydrate oxidation through hydroxyl radical attacks [2,46]. However, this reaction pathway often results in sensors of this type suffering from low selectivity; this will be further addressed in the chronoamperometric analysis below. The formation of hydroxyl radicals via surface adsorbed OH^- have been extensively studied [47–49]. The reduction potential of surface bound OH radicals is far less than the $OH^-/\bullet OH$ redox couple thus providing additional evidence for the mechanism proposed in Fig. 7B. In both the light and dark conditions, the shape of the CV curves remained similar, though the peak currents differed. It is thus entirely plausible that during illumination there is an additional generation of oxidative •OH species over and above the oxidation occurring via the Cu (II)/Cu(III) couple. This would explain the increase in current density seen in the light as more electrons would be excited into the conduction band of the CuO photoelectrode thus increasing the conductivity.

The kinetic interactions occurring at the electrode's interface allow for more meaningful conclusions regarding the glucose oxidation process. Fig. S4A reveals how the oxidation potential and ultimately peak current variation with scan rate, measured at 25, 30, 40, 50, 70, 100, 150, 175, 200 and 300 mV/s in a solution containing 1 mM glucose and 0.1 M NaOH. A shift in potential to more positive oxidative levels is observed with increasing scan rate suggesting that the glucose oxidation process is irreversible whilst the Cu(II)/Cu(III) redox couple is electrochemically reversible. A plot (Fig. S4B - 1) of peak potential vs log (υ) revealed a slope of 57.5 mV/decade further supporting the theory that an irreversible electron transfer process is the reason for the oxidation peaks during the anodic scan. Also, no reduction peaks are formed at potentials lower than the oxidation potential (0.6 V vs. Ag/AgCl) confirming the irreversible nature. There is a strong linear dependence between the peak current (i_p) and square root of the scan rate ($\sqrt{\nu}$) with a regression coefficient of $R^2 = 0.999$ in the dark. Similarly, a strong linear relationship was found between $i_p and \sqrt{\nu}$ which retained a regression coefficient of $R^2 = 0.993$ in the light. The etched CuO sample sowed a slope of 61.4 mV/decade in the light as depicted in Fig. S4B - 2. These dependencies in both the light and dark indicate that the oxidation of glucose at this CuO electrode is a mass transfer process within the double layer controlled by diffusion of glucose to the active redox sites. Also, these findings rule out the possibility of a quasi-reversible system as in such processes, linearity between $i_p and \sqrt{\nu}$ is not found. Anodic shifts were also noted to increase potentials with increasing scan rate in the light (Fig. S4C). The difference, however, is the magnitude of anodic current, which is far greater than in the dark with all other parameters equal. The cathodic scan also reveals little change in peak potentials; however, these were more easily distinguishable. This may be due to a difference in the kinetic rate constant. The electrochemical rate constants (k_o) for this system could not be assessed via CV experiments as the formal potential (E^0) for this glucose/CuO system was not obtainable [50]. Alternatively, the rate constants can be predicted by making use of EIS measurements. For each of the scan rates in the light and dark conditions, the peak oxidation potentials (E_p) were assessed along with the half peak potentials ($E_{p/2}$) which are recorded in Table 1 and 2. For an irreversible mass transport-controlled system the diffusion coefficient was assessed using the Equations (10) and (11), where the electrochemical transfer coefficient must first be calculated. In both the light and dark, the diffusion coefficient decreased exponentially with increasing scan rate as depicted in Fig. S5. This decrease is due to the depletion of the diffusion layer at higher scan rates. From the CVs conducted at various scan rates the mean diffusion coefficients in the light and dark were 1.8×10^{-5} cm^2/s and 3.3×10^{-5} cm^2/s respectively. These values are in good agreement with literature [51–53]. An increase in the mean diffusion coefficient was noted in transitioning from the dark to light condition. This is ascribed to the presence of additional charge carriers (e^-/h^+) present at the electrodes surface which assist in the glucose oxidation process.

Table 1
Important electrochemical parameters deduced at various scan rates in the dark.

Scan Rate, υ in mV/s	i_p, in mA	E_p, in V	$E_{p/2}$, in V	α	D_o
25	1.086	0.554	0.396	0.301	7.02E-05
30	1.108	0.542	0.398	0.331	4.60E-05
40	1.146	0.579	0.400	0.268	3.43E-05
50	1.201	0.552	0.403	0.320	2.01E-05
70	1.303	0.559	0.410	0.320	1.21E-05
100	1.413	0.562	0.415	0.326	6.86E-06
125	1.489	0.569	0.420	0.320	4.96E-06
150	1.571	0.579	0.425	0.310	3.95E-06
175	1.636	0.586	0.430	0.305	3.20E-06
200	1.696	0.583	0.432	0.315	2.55E-06
300	1.885	0.601	0.442	0.301	1.47E-06

Table 2
Important electrochemical parameters deduced at various scan rates in the light.

Scan Rate, υ in mV/s	i_p, in mA	E_p, in V	$E_{p/2}$, in V	α	D_o
25	1.367	0.601	0.403	0.241	1.39E-04
30	1.383	0.579	0.400	0.268	8.88E-05
40	1.399	0.559	0.398	0.296	4.62E-05
50	1.469	0.549	0.403	0.326	2.97E-05
70	1.644	0.576	0.410	0.287	2.15E-05
100	1.795	0.576	0.420	0.305	1.18E-05
125	1.946	0.583	0.427	0.305	8.88E-06
150	2.008	0.598	0.432	0.287	6.98E-06
175	2.151	0.598	0.437	0.296	5.71E-06
200	2.228	0.601	0.442	0.301	4.62E-06
300	2.439	0.601	0.449	0.315	2.35E-06

$$\left(E_p - E_{p/2}\right) = \frac{1.857RT}{\alpha F} \tag{10}$$

$$D_o = \left(\frac{i_p}{\left(2.99 \times 10^5\right)\alpha^{0.5} A C_o D_o^{0.5} \upsilon^{0.5}}\right)^2 \tag{11}$$

3.5. Effect of glucose concentration

Fig. S6 shows cyclic voltammograms of the "etched" CuO photoelectrode in the presence of various concentrations of glucose in the dark and light at a 100 mV/s scan rate. A typical electrochemical response was recorded under both conditions. Upon increasing the glucose concentration, the anodic peaks shift toward higher oxidative potentials. Similarly, the positive sweep peak currents increased with glucose concentration. The onset potential remained mostly unchanged regardless of glucose concentration. Also, the semiconductive properties of the "etched" CuO film is showcased with vastly greater oxidation peak currents in the light as opposed to the dark under the same conditions. Under illumination, the 5 mM glucose response lost its characteristic oxidation peak and appeared to be saturated. In contrast, the dark CV presented clearly visible oxidation peak however, above 5 mM glucose, the CV responses were completely saturated showing no clear oxidation peaks.

3.6. Charge carrier transport assessment

The electrochemical impedance characterization of selected samples was carried out in a solution of 0.1 M NaOH with various glucose concentrations both in the dark and under illumination. The impedance measurements were used to construct Nyquist plots over a range of glucose concentrations as presented in Fig. 8. Here, the shape of Nyquist plots varies drastically between the light and dark condition. In the dark, the Nyquist plots displayed flattened and incomplete capacitive arcs

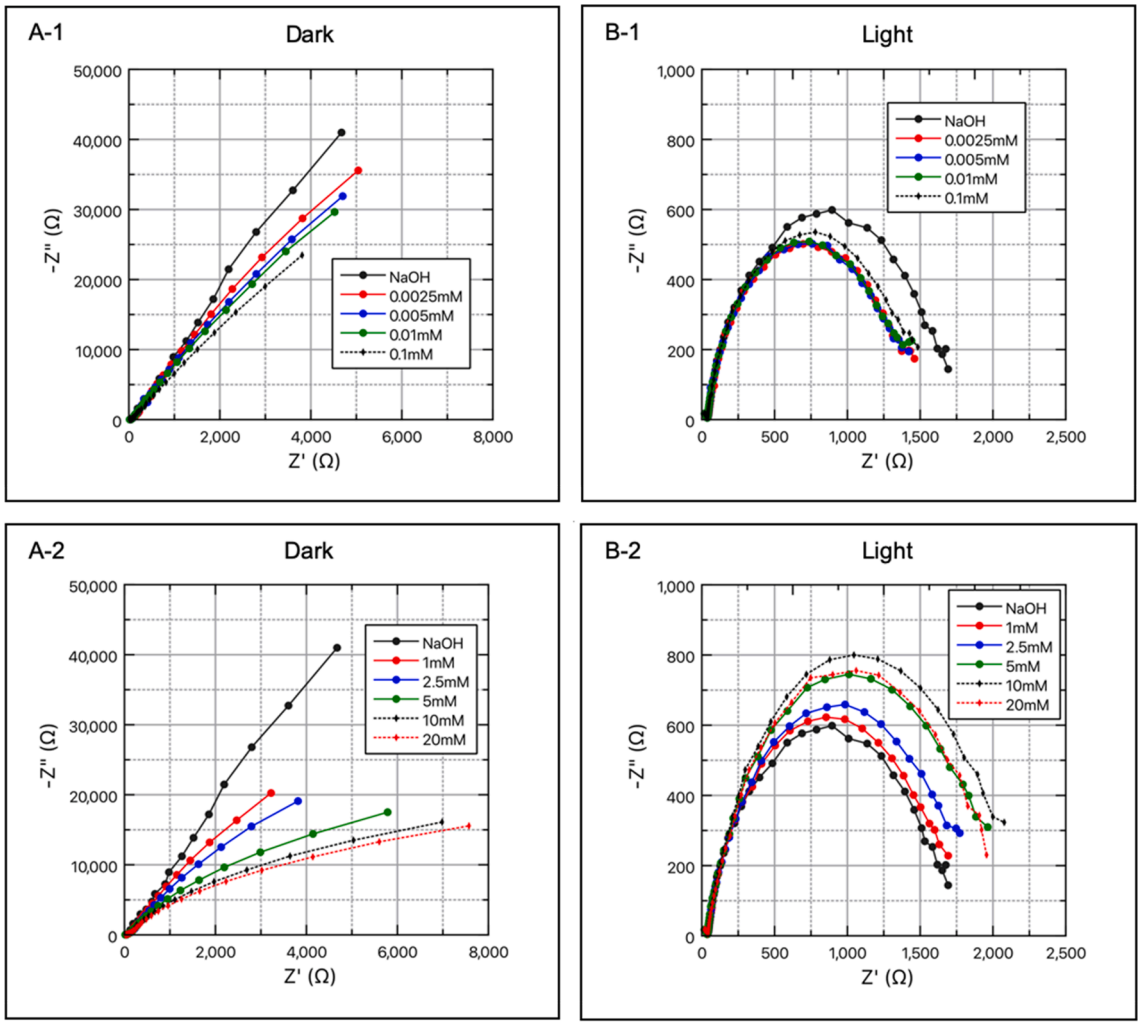

Fig. 8. Nyquist plots in the dark (A-1 and A-2) and under illumination (B-1 and B-2) over a range of glucose concentrations.

which decrease in size with increasing glucose concentration. Typically, this feature is associated with the formation of a passive film over the surface of the electrode. In the light this is only true at low concentrations where at concentrations above 1 mM, the diameter of the Nyquist plot increases. The charge transfer mechanism is much more complex in the light. Under illumination, higher glucose concentrations produce a larger barrier to interfacial charge transfer which may be due to decreased OH^- ion concentration near the surface of the electrode. Under illumination, a clear depressed semi-circle is visible both in the presence and absence of glucose. The semi-circle peak in the medium frequency range increases with glucose concentration suggesting higher charge transfer resistances between the solid and electrolyte interface (R_{CT}). The analysis of Nyquist plots in the high and medium frequency region is especially complex and to accurately interpret charge carrier transport, an appropriate equivalent circuit must be used to fit the EIS data. Previously, Yang et al.,(2018) Meng and Liu (2019) made use of a modified Randel's circuit with a double parallel arrangement to depict EIS data in an equivalent circuit for two-time constants [54,55]. Due to the grain-like morphology and nature of the coating, the circuit presented in Fig. S7 was used to further interpret the EIS data as the diffusion paths are similar. From the electrical equivalent circuit, R_s represents the solution resistance, R_C and C_c denote the coating resistance and capacitance respectively whereas C_{dl} is the double layer capacitance and R_{CT} is the charge transfer resistance. The capacitive elements were replaced with constant phase elements (CPE) to account for the scattering effect as a result of surface heterogeneity [56]. It is common practice to make use of CPE's as the electrochemical responses are believed to be purely capacitive in nature. The aforementioned circuit was used to fit both the light and dark scenarios with great success. The equation derived from this circuit including CPE components is complex though after some work simplifies to Equation (12).

$$Z_{Circuit} = R_s + \frac{(CPE_{11}X_{Real} - CPE_{12}X_{imag}) + j(CPE_{12}X_{Real} + CPE_{11}X_{imag})}{(CPE_{11} + X_{Real}) + j(CPE_{12} + X_{imag})} \quad (12)$$

Using the overall circuit equation upon separating the real from the imaginary, the fitting parameters were found using Microsoft excel and Excel's Solver add-in. The results are tabulated (Table S2: Dark, Table S3: Light) for both the light and dark conditions under various glucose concentrations. The difference in charge transfer resistance between the light and dark condition is staggering with the light condition enjoying (R_{CT}) which are several orders of magnitude smaller. In the dark, the charge transfer resistance (R_{CT}) fluctuates slightly at low glucose concentrations (0.0025 mM to 0.025 mM) and then peaks at 0.1 mM. This indicates that between a blank solution and up to 0.1 mM, the charge transfer process is complex. By increasing the glucose concentration (0.1 mM to 20 mM) the charge transfer resistance decreases to levels below that of the blank solution indicating a more favorable charge transfer process. In the light however, the R_{CT} decreases from 1634 Ω/cm^2 in a blank solution until a minimum is reached at 1377 Ω/cm^2 for 0.005 mM glucose. The R_{CT} then increases steadily to 2146 Ω/cm^2 in 15 mM glucose before decreasing again. The surface

heterogeneity factor in both the light and dark are close to $n = 1$ indicating good surface exposure to the electrolyte.

Upon closer inspection of both the light and dark conditions in a 1 mM glucose testing solution, a smaller depressed semicircle is observed as a tail in the high frequency region as per Fig. 9. This high frequency region semi-circle is attributed to the resistance of the surface passivating layer [57]. The Bode-modulus plot reveals constant phase behavior in the middle and high frequency region in the dark. Conversely, in the light, this constant phase behavior is reduced significantly in the lower end of the high frequency range. According to the Bode-phase plot, one-time constant is observed in the high frequency region and another in the mid frequency region. The latter corresponds to the charge transfer reaction whereas the former represents the properties of the passive film form on the surface during testing [54]. In both dark and light, the solution resistance (R_s) fluctuates. These deviations can be attributed to inhomogeneous mixing following the addition of glucose to the testing solution. It was expected the solution resistance would increases with increased glucose concentration as glucose does not dissociate into its ions making it a poor conductor in solution. This, however, is not the case as the concentrations used are so limited it has little effect on the solution resistance. Finally, the relationship between glucose concentration and charge transfer resistance could not be established and cannot be used detect glucose accurately.

An investigation into the determination of k^o via EIS as oppose to CV was conducted by Edward P. Randviir who found that both approaches are comparable [58]. Due to the irreversible nature of the reaction between glucose and CuO, an accurate determination of the standard reduction potential is not possible and hence was rather be examined via EIS. As such, the R_{CT} is related to the exchange current (i_o) and subsequently the heterogeneous electron transfer rate (k^o) by the expressions:

$$R_{CT} = \frac{RT}{nFi_o} \tag{13}$$

$$i_o = nFAC_o k^o \tag{14}$$

where R is the universal gas constant, T is the temperature, n is the number of electrons (can be considered as = 1) and F which is Faraday's number. By applying these equations, the mean electron kinetic transfer rate over a glucose concentration range of 0.1 mM to 20 mM, was found to be 9.7E-08 cm/s and 3.46E-04 cm/s in the dark and light respectively. These k^o values align well with other reports using CV measurements as oppose to EIS thus further confirming the findings by Randviir and others [52,58,59].

3.7. Chronoamperometric glucose detection

The chronoamperometric detection of glucose was carried out to determine the current response of the CuO photoelectrode samples to successive glucose injections. From the CV's, the E_p occurred between 0.55 V and 0.60 V which was subsequently used as the applied potentials for the analysis in the dark and light. An interval time of 50 s between each successive glucose addition was used under constant stirring in 0.1 M NaOH solution. Though this interval time is long, the time taken to reach a steady state current was rapid. The peak currents were determined using CVs in solution containing 1 mM glucose in 0.1 M NaOH. This means that the peak potentials were found for this particular concentration of glucose not a range. As a result, independent chronoamperometric studies were conducted under 0.55 V, 0.57 V and 0.6 V bias. Upon finetuning the applied voltage, the largest difference between light and dark current density was achieved at 0.55 V as presented in Fig. S8. Over the range of applied potentials, the iconic staircase rise in

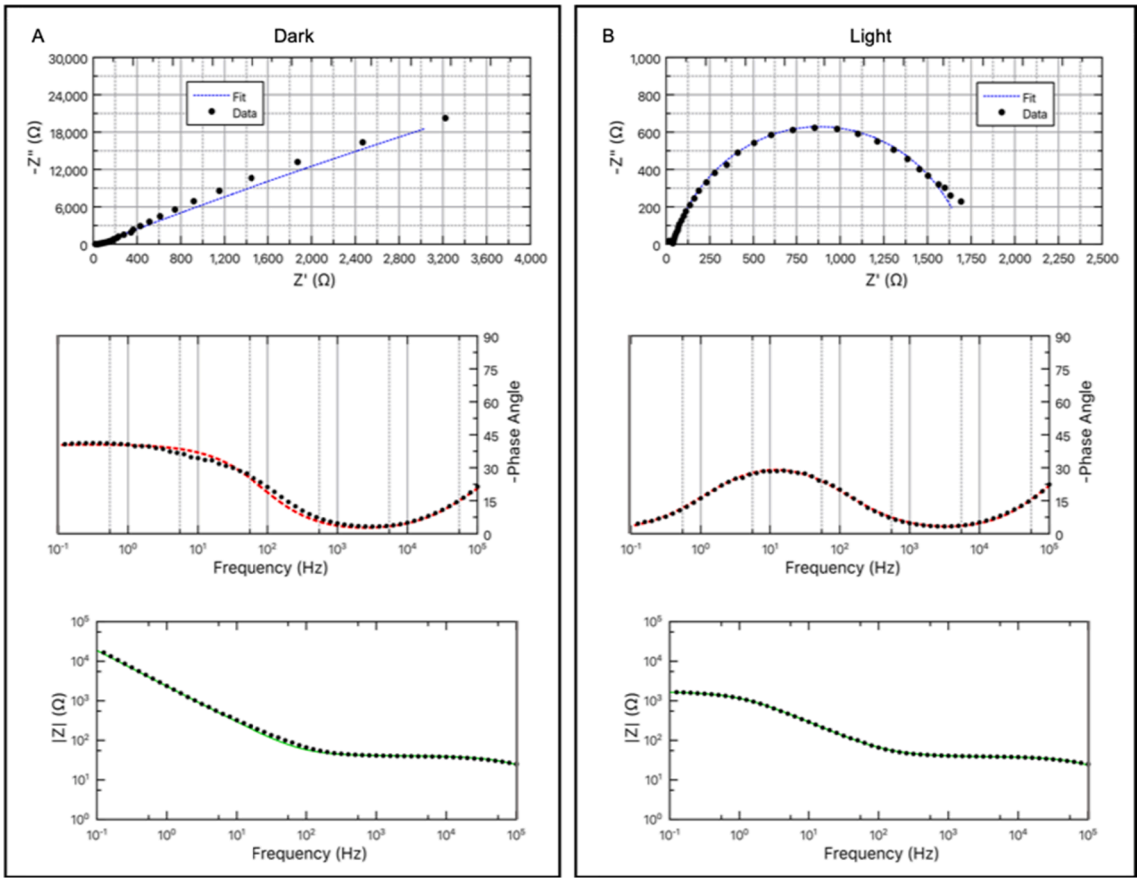

Fig. 9. Zoomed in view of fitted high frequency Nyquist and Bode plots using the modified Randel's circuit in A) Dark and B) Light for 1 mM glucose.

current was evident in the dark and light. As the applied voltage is increased, the difference between light and dark current decreased. This suggests the possibility of a maximum current difference between the dark and light scenario as seen in the CV measurements. The chronoamperometric data in Fig. S8 shows that glucose detection in concentration levels below 0.41 mM show no significant difference between the dark and illuminated samples. Above this concentration, the semiconductive behavior of the CuO photoelectrode become apparent with higher current responses to the same glucose concentration. The divergence between the recorded current and the glucose concentration measured in the dark and light continued to grow even after an addition of 20 mM glucose. A closer inspection of the 0.60 V "etched" sample's chronoamperometric response in Fig. S9 confirms that the difference between light and dark only become apparent following the addition of 0.41 mM of glucose. After this critical point, the difference continued to grow even after the highest glucose concentration injection. Impressively fast response times of 4 s were recorded for both the dark and light tests indicating that light had no influence on the time taken to respond to glucose additions.

The peak currents following each successive glucose injection were determined and plotted against the respective glucose concentrations to develop a calibration curve. Fig. 10 shows this calibration curve for the "etched" CuO sensor in the light and dark. A total of 3 linear ranges (LR-1, LR-2 and LR-3) are clearly identified under both scenarios with strong correlation coefficients. LR-1 covers a 0–2.77 mM glucose range, LR-2 spans across 2.77–9.95 mM and LR-3 covers the largest range between 9.95 mM and 29.12 mM glucose. These linear ranges were not altered by the inclusion of light in the system however, the correlation coefficients of LR-1 are seen to increase from dark to light and decrease for the LR-2 range. The increased oxidation current of the optimized CuO thin film also had no effect on the linear ranges. With smaller formations on the surface of the etched electrode, the surface area is increased. This increase in surface area has been reported to cause small increases in linear range though coupled with good adhesion to the FTO substrate, the linear range is further enhanced. The major contribution to the increased linear range is believed to be due to the enhanced electronic properties and more specifically charge carrier mobility and conductivity. With such high conductivities, charge carrier separation is easily attainable. The sensitivity and limit of detection, however, were greatly influenced by illumination. The sensitivity in the dark was found to be $197\mu A/mMcm^2$, whereas in the light, it increased to $263\mu A/mMcm^2$. The low sensitivity could be attributed to the described high charge carrier concentration. This is supported by numerous reports concerning semiconductors having decreased sensitivity as a result of increased charge carrier density [59–61]. Additionally, the LOD at (S/N) of 3 decreased from 0.079 to 0.059 *mM* showing enhanced lower detection limits under illumination. The detection properties for this sensor are highly comparable with many works as presented in Table S4.

As such, to mimic the constituents found in human blood the interfering species (Fructose, Sucrose, NaCl, Uric Acid, Citric Acid, Ascorbic Acid, Acetaminophen) were added in 100 s intervals to a testing solution containing 0.1 M NaOH. Fig. 11 A shows the current/time characteristics associated with the addition of these interfering species. The results from the interference study showed that even closely related monosaccharides such as fructose (isomeric to glucose) and sucrose did not result in any significant response at levels similar to those present in human blood. An addition of 0.1 mM uric acid (UA) produced the greatest interference with the CuO thin film with a decrease of almost 0.1 mA/cm^2. This interference is ascribed to the anionic nature of the UA which causes a decrease in current density. The addition of light caused no changes in the sensor's response toward interfering species. A common cause for interference and catalyst poisoning comes in the form of Cl, however, this work showed no Cl poisoning, even at very high NaCl levels. Overall, the response to glucose was significant before and after the introduction of interfering species which makes this "etched" CuO thin film a promising non-enzymatic biosensor.

The reproducibility of the etched CuO thin film was electrochemically tested using CV in a solution of 0.1 M NaOH and 1 mM Glucose. Samples were first stabilized at a scan rate of 100 mV/s for ten cycles and the data was recorded at 50 mV/s. Anodic peak current densities of the five prepared samples were recorded at 0.54 V vs Ag/AgCl. The reproducibility of the etched CuO films is represented in Fig. 11 B. This shows excellent electrode reproducibility in both the light (RSD = 4.85%) and dark (RSD = 1.86%) scenarios. The shelf life of the CuO electrode was validated under the same conditions as those used for the reproducibility test (Fig. 11C). An etched sample was selected and repeatedly tested over a period of one month (1-day, 2-days, 4-days, 7-days, 14-days, 21-days, and 28-days). The results depicted in Fig. 11C reveal that in the dark the deterioration was subtle with the largest photocurrent decrease (0.026 mA/cm^2) occurring between 2 and 4 days. In the light however, clear evidence of photo-corrosion is seen with much larger deterioration over the same time frame. The RSD's for the dark and light condition were found to be 2.40% and 4.56% respectively. Under these same conditions, one electrode was subjected to repeated CV cycles to assess the repeatability of the anodic peaks obtained. As per Fig. 11D, it was found that the oxidation peaks for this sample were very repeatable over

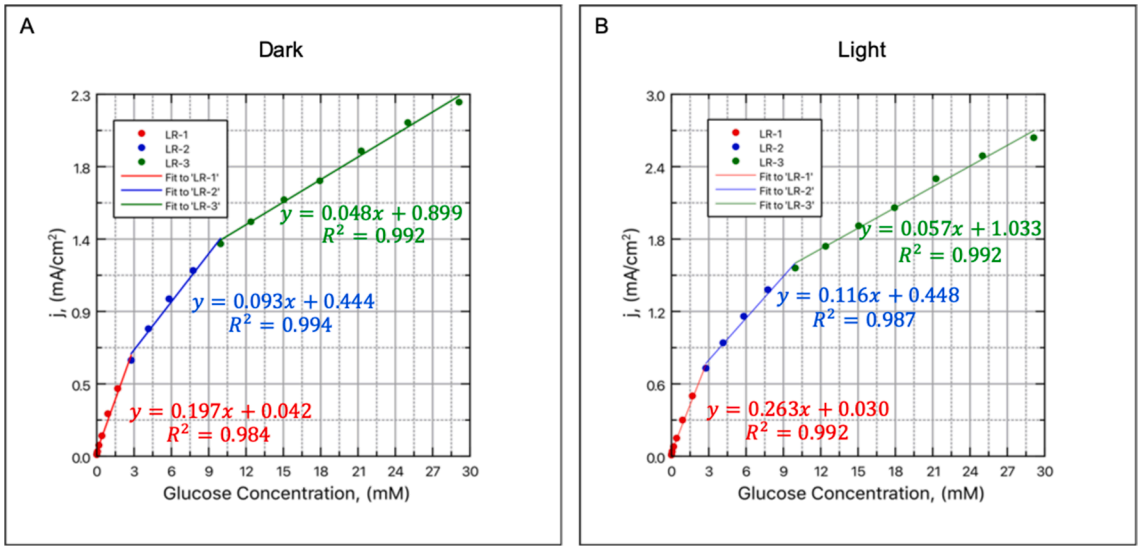

Fig. 10. Calibration curve for the "Etched" CuO thin film depicting 3 linear ranges in the A) Dark and B) light.

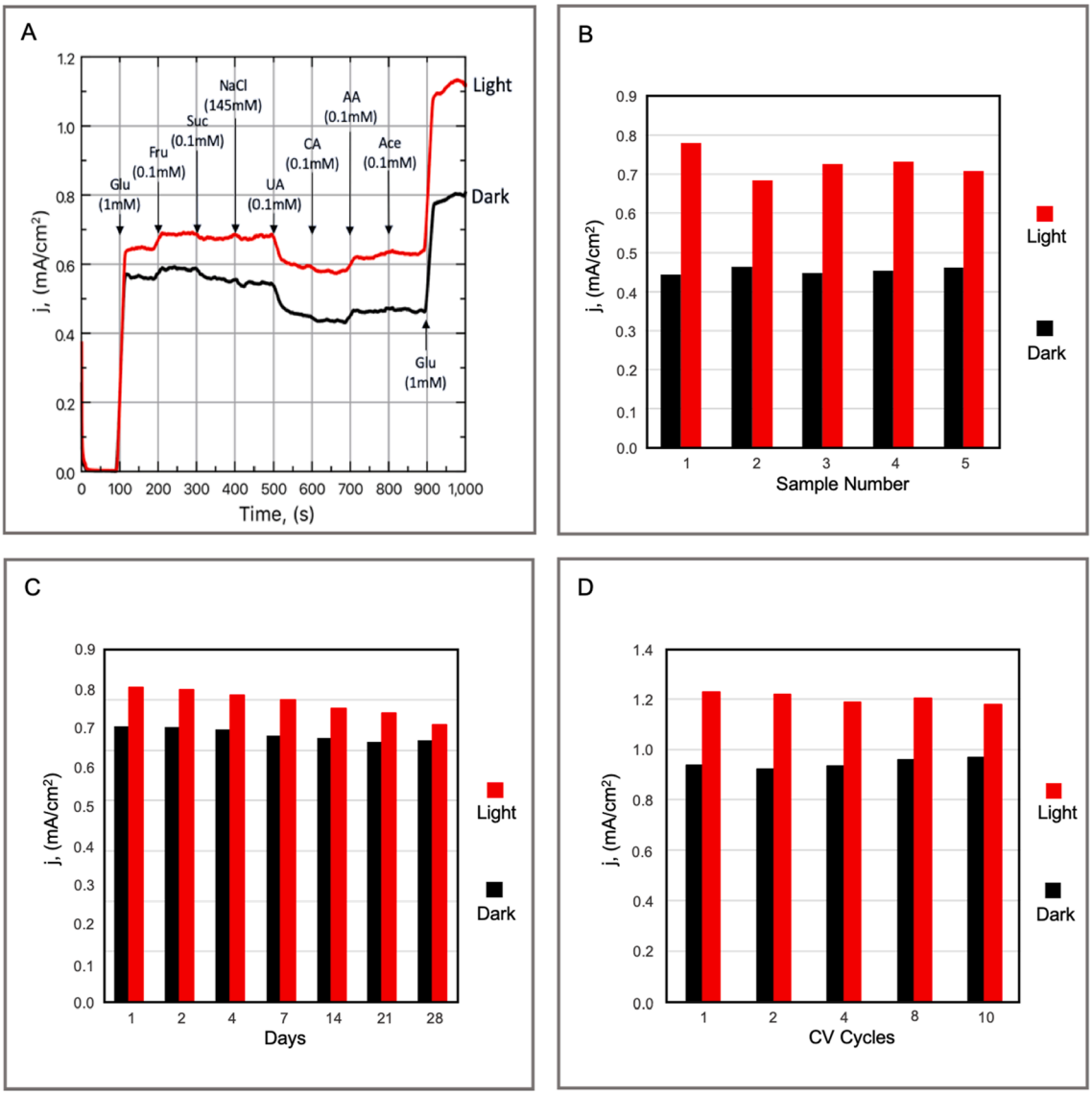

Fig. 11. A) Chronoamperometric response to common interfering species on the "etched" CuO electrode in the dark and light, B) Electrode reproducibility test for five samples in light and dark conditions, C) Etched CuO photoelectrode Shelf-life assessment and D) Peak anodic currents for a series of 10 CV cycles on the same etched CuO sample illustrating repeatability.

10 Cycles for both the dark and light with RSD's of 1.98% and 1.75% respectively.

3.8. Transient photocurrent

The recombination characteristics of charge carriers for the glucose sensor was evaluated under chopped light conditions. A three-electrode system was used in an optical glass box containing a range of glucose concentrations and 0.1 M NaOH. The AutoLab software was set to turn the LED on and off at regular intervals during the testing phase at an applied voltage of 0.54 V vs Ag/AgCl. Fig. 12 shows the intermittent illumination of the "etched" CuO photoelectrode which revealed a sharp increase in current the moment the semiconductor was exposed to light. At low glucose concentrations, a characteristic hump was formed during the first 5 s of illumination followed by a much slower current increase to its respective steady state. This initial spike can be attributed to the generation of electrons and holes which act in tandem with the Cu(III) species to rapidly oxidize glucose. Transients arise from the perturbations imposed on the system and the photogenerated charge results in a current which is measured against time. The time difference between the old and new system equilibrium states can be used to define the transport parameters. The photogenerated transients were modelled using the triphasic stretched exponential function as follows:

$$I = i_o + A_1\left(e^{\frac{-t}{\tau_1}}\right) + A_2\left(e^{\frac{-t}{\tau_2}}\right) + A_3\left(e^{\frac{-t}{\tau_3}}\right) \quad (15)$$

Here, A represents a dimensionless weighting parameter associated with the amplitude of the photoinduced response, t denotes the time, i_o represents the dark current and τ is the RC time constants for each exponential term in agreeance with previous works [62–64]. The triphasic nature of the chopped light response indicates the presence of non-interacting charge carriers which act to shift the fermi energy level via their unique decay pathway. Furthermore, the rise and decay profiles reveal that the CuO photoelectrode is controlled via multiple processes which together result in its overall persistent photocurrent (PPC) behavior. The concentration of glucose altered both the shape and intensity of the current rise and decay curves. At low concentrations up to 1 mM, the electron-hole recombination appeared prevalent though upon increasing the amount of glucose in the system, the charge carrier elimination effects became less obvious. The parameters during the rise

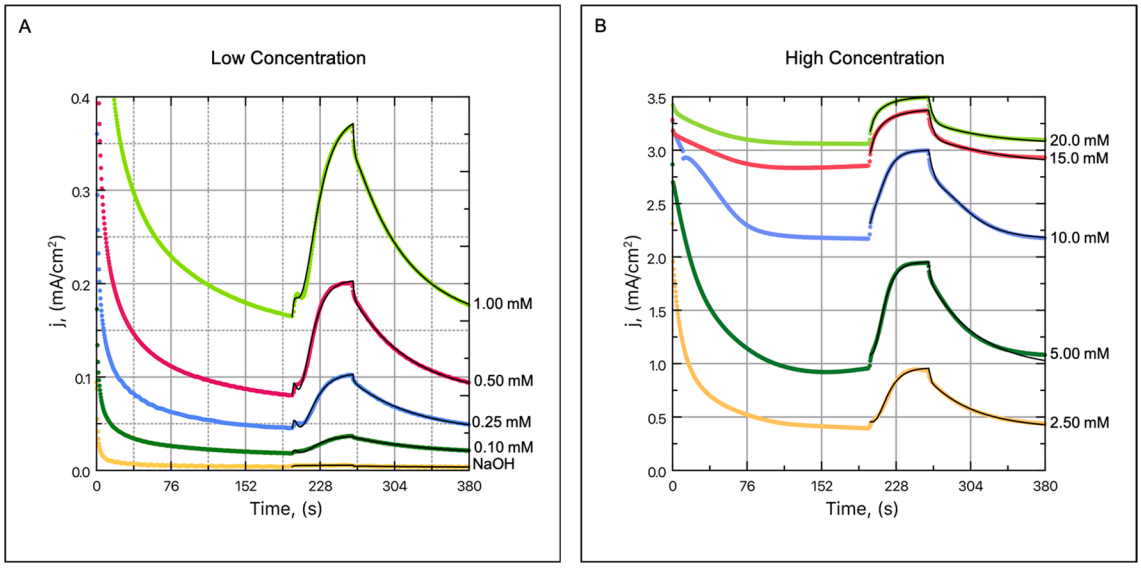

Fig. 12. Light chopping at a 0.54 V bias for A) Low concentrations (NaOH, 0.1, 0.25, 0.5, 1.0 mM Glucose) and B) High Concentrations (2.5, 5.0, 10.0, 15.0, 20.0 mM Glucose).

A_1 and τ_{1R} in the above equation arise due to the initial spike which is attributed to the electron-hole pair recombination. A slower increase in photocurrent following this spike is due to the adsorption of OH– to the surface active CuO sites. This gradual rise follows PPC behavior that lasts much longer than the initial spike. The diminishing rise of current until the light cut-off point confirms that A_{2R}/A_{3R} and τ_{2R}/τ_{3R} are associated with the adsorption processes. Following the termination of the light source the current slowly dissipates though never attains its starting current even after 130 s post illumination. This decay is attributed to a combination of desorbing species as well as oxidation products leaving the surface vicinity. This slow dissipation after illumination is highly characteristic for systems which experience persistent photocurrent as a result of limited interaction at deep trap states with re-adsorbed species [65]. The previously excited electrons energy is decreased to levels before illumination causing them to rejoin the VB and fulfilling Shockley-Read Hall recombination. Interestingly, it can be noted that the rising time constant τ_{2R} with glucose concentration is much faster than for the decay time constant. Conversely, the decay time constants τ_{1D} and τ_{3D} are faster for the decay region than in the rise for increasing concentrations. It is this comparably fast adsorption process which results in the drastic increase in glucose oxidation when light is incident on the CuO photoelectrode. The fitting parameters used are displayed in the supplementary Tables S5 and S6.

4. Conclusion

In this study a photo active thin film CuO was electrodeposited onto FTO. Wet-chemical etching of the electrodeposited thin film allowed band gap tuning of the deposited thin film. During glucose oxidation, the shape of the CV curves in the dark and light remained unchanged. Under illumination, the oxidation peak current was greatly enhanced as compared to dark conditions. Glucose oxidation at the electrodes surface is diffusion controlled. The PEC glucose oxidation mechanism followed similar oxidation pathways as in the dark however, it was suspected to be a combination of Cu(II)/Cu(III) and hydroxyl radicals, produced following charge separation, that is believed to be responsible for the increase current density. A higher kinetic rate constant and diffusion coefficient were obtained for the illuminated samples. In addition, lower charge transfer resistances were found in the light than in the dark. Also, under transient illumination, it was determined that deep trap states resulted in the formation of persistent photoconductivity. Chronoamperometric measurements revealed that the linear range of detection was unaffected by the increased current density in the light though the sensitivity and LOD were enhanced. A very large linear range (up to 29 mM) was found. In both light and dark, the selectivity toward glucose was phenomenal with very little interference from a wide range of interfering substances.

Declaration of Competing Interest

The authors declare that they have no known competing financial interests or personal relationships that could have appeared to influence the work reported in this paper.

Acknowledgements

The authors would like to thank the National Research Foundation (NRF) South Africa and the Cape Peninsula University of Technology for financial grant (NRF Grant: 117686, and CPGS postdoctoral fellowship 2021).

Appendix A. Supplementary material

Supplementary data to this article can be found online at https://doi.org/10.1016/j.apsusc.2021.151822.

References

[1] Barrett, Public Health Ethics: Cases Spanning the Globe, Springer International Publishing, 2016.
[2] J.T.C. Barragan, S. Kogikoski, E.T.S.G. Da Silva, L.T. Kubota, Insight into the Electro-Oxidation Mechanism of Glucose and Other Carbohydrates by CuO-Based Electrodes, Anal. Chem. 90 (2018) 3357–3365, https://doi.org/10.1021/acs.analchem.7b04963.
[3] E. Sehit, Z. Altintas, Significance of nanomaterials in electrochemical glucose sensors: An updated review (2016–2020), Biosens. Bioelectron. 159 (2020) 112165, https://doi.org/10.1016/j.bios.2020.112165.
[4] K. Tian, K. Baskaran, A. Tiwari, Nonenzymatic glucose sensing using metal oxides – Comparison of CuO, Co3O4, and NiO, Vacuum 155 (2018) 696–701, https://doi.org/10.1016/J.VACUUM.2018.06.060.
[5] M.M. Rahman, A.J.S. Ahammad, J.-H. Jin, S.J. Ahn, J.-J. Lee, A Comprehensive Review of Glucose Biosensors Based on Nanostructured Metal-Oxides, Sensors. 10 (2010) 4855–4886, https://doi.org/10.3390/s100504855.
[6] D.M. Tobaldi, C. Espro, S.G. Leonardi, L. Lajaunie, M.P. Seabra, J.J. Calvino, S. Marini, J.A. Labrincha, G. Neri, Photo-electrochemical properties of CuO–TiO2 heterojunctions for glucose sensing, J. Mater. Chem. C. 8 (2020) 9529–9539, https://doi.org/10.1039/D0TC01975E.
[7] H. Li, J. Li, D. Chen, Y. Qiu, W. Wang, Dual-functional cubic cuprous oxide for non-enzymatic and oxygen-sensitive photoelectrochemical sensing of glucose, Sensors

Actuators B Chem. 220 (2015) 441–447, https://doi.org/10.1016/j.snb.2015.05.110.
[8] W. Zhan, Z. Chen, J. Hu, X. Chen, Vertical CuO nanowires array electrodes: Visible light sensitive photoelectrochemical biosensor of ethanol detection, Mater. Sci. Semicond. Process. 85 (2018) 90–97, https://doi.org/10.1016/j.mssp.2018.06.002.
[9] S. Thenmozhi, N. Dharmaraj, K. Kadirvelu, H.Y. Kim, Electrospun nanofibers: New generation materials for advanced applications, Mater. Sci. Eng. B Solid-State Mater. Adv. Technol. 217 (2017) 36–48, https://doi.org/10.1016/j.mseb.2017.01.001.
[10] L. Wang, K. Han, M. Tao, Effect of Substrate Etching on Electrical Properties of Electrochemically Deposited CuO, J. Electrochem. Soc. 154 (2) (2007) D91, https://doi.org/10.1149/1.2404913.
[11] C. Zhu, M.J. Panzer, Etching of electrodeposited Cu2O films using ammonia solution for photovoltaic applications, Phys. Chem. Chem. Phys. 18 (9) (2016) 6722–6728, https://doi.org/10.1039/C5CP06385J.
[12] C.H.M. van Oversteeg, M. Tapia Rosales, K.H. Helfferich, M. Ghiasi, J.D. Meeldijk, N.J. Firet, P. Ngene, C. de Mello Donegá, P.E. de Jongh, Copper sulfide derived nanoparticles supported on carbon for the electrochemical reduction of carbon dioxide, Catal. Today 377 (2021) 157–165, https://doi.org/10.1016/j.cattod.2020.09.020.
[13] Z. Li, Y. Xin, Z. Zhang, H. Wu, P. Wang, Rational design of binder-free noble metal/metal oxide arrays with nanocauliflower structure for wide linear range nonenzymatic glucose detection, Sci. Rep. 5 (2015) 1–10, https://doi.org/10.1038/srep10617.
[14] F. Parmigiani, L.E. Depero, T. Minerva, J.B. Torrance, The fine structure of the Cu2p3 2 X-ray photoelectron spectra of copper oxide based compounds, J. Electron Spectros. Relat. Phenomena. 58 (4) (1992) 315–323, https://doi.org/10.1016/0368-2048(92)85017-2.
[15] L. Debbichi, M.C. Marco De Lucas, J.F. Pierson, P. Krüger, Vibrational properties of CuO and Cu 4O 3 from first-principles calculations, and raman and infrared spectroscopy, J. Phys. Chem. C. 116 (2012) 10232–10237, https://doi.org/10.1021/jp303096m.
[16] Nagajyothi, Co_3O_4 nanoparticles as a high-performance, Phys. Chem. Chem. Phys. 18 (2015) 926–931.
[17] M.R. Joya, J. Barba-Ortega, A.M. Raba, Vibrational Raman modes and particle size analysis of cupric oxide with calcination temperature, Indian J. Pure Appl. Phys. 57 (2019) 268–271.
[18] T.H. Tran, V.T. Nguyen, Copper Oxide Nanomaterials Prepared by Solution Methods, Some Properties, and Potential Applications: A Brief Review, Int. Sch. Res. Not. 2014 (2014) 1–14, https://doi.org/10.1155/2014/856592.
[19] Y. Su, Copper Oxide Nano Photocatalyst for Wastewater Purification using Visible Light, University of Cambridge (2018), https://doi.org/10.17863/CAM.25069.
[20] J. Wu, B. Yin, F. Wu, Y. Myung, P. Banerjee, Charge transport in single CuO nanowires, Appl. Phys. Lett. 105 (18) (2014) 183506, https://doi.org/10.1063/1.4900966.
[21] A. Yabuki, N. Arriffin, Electrical conductivity AR of copper nanoparticle thin films annealed at low temperature, Thin Solid Films 518 (2010) 7033–7037, https://doi.org/10.1016/j.tsf.2010.07.023.
[22] D. Li, J. Hu, R. Wu, J.G. Lu, Conductometric chemical sensor based on individual CuO nanowires, Nanotechnology. 21 (48) (2010) 485502, https://doi.org/10.1088/0957-4484/21/48/485502.
[23] M.E. Grigore, E.R. Biscu, A.M. Holban, M.C. Gestal, A.M. Grumezescu, Methods of synthesis, properties and biomedical applications of CuO nanoparticles, Pharmaceuticals. 9 (2016) 1–14, https://doi.org/10.3390/ph9040075.
[24] L. De Los Santos Valladares, D.H. Salinas, A.B. Dominguez, D.A. Najarro, S. I. Khondaker, T. Mitrelias, C.H.W. Barnes, J.A. Aguiar, Y. Majima, Crystallization and electrical resistivity of Cu 2O and CuO obtained by thermal oxidation of Cu thin films on SiO 2/Si substrates, Thin Solid Films 520 (20) (2012) 6368–6374, https://doi.org/10.1016/j.tsf.2012.06.043.
[25] J. Morasch, H.F. Wardenga, W. Jaegermann, A. Klein, Influence of grain boundaries and interfaces on the electronic structure of polycrystalline CuO thin films, Phys. Status Solidi Appl. Mater. Sci. 213 (6) (2016) 1615–1624, https://doi.org/10.1002/pssa:v213.610.1002/pssa:201533018.
[26] L.S. Parenr, A.J. Bard, A.B. Bocarsly, F.F. Fan, E.G. Walton, M.S. Wrighton, Of the american chemical society, 102 (1980).
[27] R. Li, Y. Zhou, M. Sun, Z. Gong, Y. Guo, F. Wu, W. Li, W. Ding, Influence of Charge Carriers Concentration and Mobility on the Gas Sensing Behavior of Tin Dioxide Thin Films, Coatings. 9 (2019) 591, https://doi.org/10.3390/coatings9090591.
[28] P. Makuła, M. Pacia, W. Macyk, How To Correctly Determine the Band Gap Energy of Modified Semiconductor Photocatalysts Based on UV-Vis Spectra, J. Phys. Chem. Lett. 9 (23) (2018) 6814–6817, https://doi.org/10.1021/acs.jpclett.8b0289210.1021/acs.jpclett.8b02892.s001.
[29] B. Maack, N. Nilius, Oxidation of polycrystalline copper films – Pressure and temperature dependence, Thin Solid Films 651 (2018) 24–30, https://doi.org/10.1016/j.tsf.2018.02.007.
[30] A. Rydosz, K. Kollbek, N.-T. Kim-Ngan, A. Czapla, A. Brudnik, Optical diagnostics of the magnetron sputtering process of copper in an argon–oxygen atmosphere, J. Mater. Sci.: Mater. Electron. 31 (14) (2020) 11624–11636, https://doi.org/10.1007/s10854-020-03713-z.
[31] W.-J. Lee, X.-J. Wang, Structural, Optical, and Electrical Properties of Copper Oxide Films Grown by the SILAR Method with Post-Annealing, Coatings. 11 (7) (2021) 864, https://doi.org/10.3390/coatings11070864.
[32] Lin, Tzu-ging, " Fabrication and photonics properties of III-V semiconductor nanowire structures" (2016). Open Access Dissertations. 671. https://docs.lib.purdue.edu/open_access_dissertations/671.
[33] D. Weatherspoon, What's a Normal Blood pH and What Makes It Change?, (2019).
[34] József.S. Pap, Łukasz Szyrwiel, On the Cu(III)/Cu(II) Redox Chemistry of Cu-Peptide Complexes to Assist Catalyst Design, Comments Inorg. Chem. 37 (2) (2017) 59–77, https://doi.org/10.1080/02603594.2016.1192541.
[35] L.-P. Xia, L. Liu, N. Deng, Y.-W. Zhu, J.-B. He, Cu(III)-independent oxidation and sensing of glucose on multi-layer stacked copper nanoparticles, Microchim. Acta 182 (7-8) (2015) 1289–1295, https://doi.org/10.1007/s00604-015-1447-2.
[36] Y. Xie, C. 0. Huber, M o m o Librodot, (2001) 5–10. doi:10.1021/ac00017a012.
[37] A. Inyang, G. Kibambo, M. Palmer, F. Cummings, M. Masikini, C. Sunday, M. Chowdhury, One step copper oxide (CuO) thin film deposition for non-enzymatic electrochemical glucose detection, Thin Solid Films 709 (2020) 138244, https://doi.org/10.1016/j.tsf.2020.138244.
[38] D.R. Lide, CRC Handbook of Chemistry and Physics, 74th Ed., CRC Press, 2005.
[39] X. Wang, C. Hu, H. Liu, G. Du, X. He, Y. Xi, Synthesis of CuO nanostructures and their application for nonenzymatic glucose sensing, Sensors Actuators, B Chem. 144 (1) (2010) 220–225, https://doi.org/10.1016/j.snb.2009.09.067.
[40] S. Felix, P. Kollu, S.K. Jeong, A.N. Grace, A novel CuO–N-doped graphene nanocomposite-based hybrid electrode for the electrochemical detection of glucose, Appl. Phys. A Mater. Sci. Process. 123 (2017) 1–9, https://doi.org/10.1007/s00339-017-1217-6.
[41] J.T. Billy, A.C. Co, Reducing the onset potential of CO2 electroreduction on CuRu bimetallic particles, Appl. Catal. B Environ. 237 (2018) 911–918, https://doi.org/10.1016/j.apcatb.2018.06.072.
[42] D. Giziński, A. Brudzisz, J.S. Santos, F. Trivinho-Strixino, W.J. Stępniowski, T. Czujko, Nanostructured anodic copper oxides as catalysts in electrochemical and photoelectrochemical reactions, Catalysts. 10 (2020) 1–38, https://doi.org/10.3390/catal10111338.
[43] J.B. Mensah, I. Delidovich, P.J.C. Hausoul, L. Weisgerber, W. Schrader, R. Palkovits, Mechanistic Studies of the Cu(OH)+-Catalyzed Isomerization of Glucose into Fructose in Water, ChemSusChem. 11 (2018) 2579–2586, https://doi.org/10.1002/cssc.201800483.
[44] J. Hirst, S. Müller, D. Peeters, A. Sadlo, L. Mai, O.M. Reyes, D. Friedrich, D. Mitoraj, A. Devi, R. Beranek, R. Eichberger, Comparative Study of Photocarrier Dynamics in CVD-deposited CuWO4, CuO, and WO3 Thin Films for Photoelectrocatalysis, Zeitschrift Fur Phys, Chemie. 234 (2019) 699–717, https://doi.org/10.1515/zpch-2019-1485.
[45] H.S. Ahn, A.J. Bard, Surface Interrogation Scanning Electrochemical Microscopy of $Ni_{1-x}Fe_xOOH$ (0, J. Am. Chem. Soc. 138 (2016) 313–318.
[46] R. Travaini, C. Marangon-Jardim, J.L. Colodette, M. Morales-Otero, S. Bolado-Rodríguez, Ozonolysis (2015), https://doi.org/10.1016/B978-0-12-800080-9.00007-4.
[47] H. Shibata, Y. Ogura, Y. Sawa, Y. Kono, Hydroxyl radical generation depending on O2 or H2O by a photocatalyzed reaction in an aqueous suspension of titanium dioxide, Biosci. Biotechnol. Biochem. 62 (12) (1998) 2306–2311, https://doi.org/10.1271/bbb.62.2306.
[48] H. Liao, T. Reitberger, Generation of free OHaq radicals by black light illumination of degussa (Evonik) P25 TiO2 aqueous suspensions, Catalysts. 3 (2013) 418–443, https://doi.org/10.3390/catal3020418.
[49] Y. Nosaka, A. Nosaka, Understanding Hydroxyl Radical (•OH) Generation Processes in Photocatalysis, ACS Energy Lett. 1 (2) (2016) 356–359, https://doi.org/10.1021/acsenergylett.6b00174.
[50] A.J. Bard, L.R. Faulkner, Electrochemical methods and applications, 2nd Editio, Wiley-Interscience, 2000.
[51] W.M. Haynes, CRC Handbook of Chemistry and Physics, 97th Ed., CRC Press, 2016.
[52] N. Sattarahmady, H. Heli, A non-enzymatic amperometric sensor for glucose based on cobalt oxide nanoparticles, J. Exp. Nanosci. 7 (5) (2012) 529–546, https://doi.org/10.1080/17458080.2010.539275.
[53] A. Raziq, M. Tariq, R. Hussian, M.H. Mehmood, M.S. Khan, A. Hassan, Electrochemical Investigation of Glucose Oxidation on a Glassy Carbon Electrode Using Voltammetric, Amperometric, and Digital Simulation Methods, ChemistrySelect. 2 (30) (2017) 9711–9717, https://doi.org/10.1002/slct.201701193.
[54] X. Yang, C. Du, H. Wan, Z. Liu, X. Li, Influence of sulfides on the passivation behavior of titanium alloy TA2 in simulated seawater environments, Appl. Surf. Sci. 458 (2018) 198–209, https://doi.org/10.1016/j.apsusc.2018.07.068.
[55] F. Meng, L. Liu, Electrochemical Evaluation Technologies of Organic Coatings, Coatings Thin-Film Technol. (2019), https://doi.org/10.5772/intechopen.79736.
[56] J.T. Zhang, J.M. Hu, J.Q. Zhang, C.N. Cao, Studies of impedance models and water transport behaviors of polypropylene coated metals in NaCl solution, Prog. Org. Coatings. 49 (4) (2004) 293–301, https://doi.org/10.1016/S0300-9440(03)00115-2.
[57] J.Y. Xiang, J.P. Tu, Y.Q. Qiao, X.L. Wang, J. Zhong, D. Zhang, C.D. Gu, Electrochemical impedance analysis of a hierarchical cuo electrode composed of self-assembled nanoplates, J. Phys. Chem. C. 115 (2011) 2505–2513, https://doi.org/10.1021/jp108261t.
[58] E.P. Randviir, A cross examination of electron transfer rate constants for carbon screen-printed electrodes using Electrochemical Impedance Spectroscopy and cyclic voltammetry, Elsevier Ltd 286 (2018) 179–186, https://doi.org/10.1016/j.electacta.2018.08.021.
[59] N. Torto, T. Ruzgas, L. Gorton, Electrochemical oxidation of mono- and disaccharides at fresh as well as oxidized copper electrodes in alkaline media, J. Electroanal. Chem. 464 (2) (1999) 252–258, https://doi.org/10.1016/S0022-0728(99)00041-8.
[60] T.S. van den Heever, W.J. Perold, The influence of resistance and carrier concentration on the output voltage of a ZnO nanogenerator, Micro Nano Syst. Lett. 1 (2013) 2–7, https://doi.org/10.1186/2213-9621-1-4.

[61] Y. Chen, X. Kong, G. Lu, D. Qi, Y. Wu, X. Li, M. Bouvet, D. Sun, J. Jiang, The lower rather than higher density charge carrier determines the NH 3 -sensing nature and sensitivity of ambipolar organic semiconductors, Mater. Chem. Front. 2 (5) (2018) 1009–1016, https://doi.org/10.1039/C7QM00607A.

[62] Z. Li, F. Gao, N.C. Greenham, C.R. McNeill, Comparison of the operation of polymer/fullerene, polymer/polymer, and polymer/nanocrystal solar cells: A transient photocurrent and photovoltage study, Adv. Funct. Mater. 21 (8) (2011) 1419–1431, https://doi.org/10.1002/adfm.v21.810.1002/adfm.201002154.

[63] V. Bhatt, M. Kumar, J. Kim, H.-J. Chung, J.-H. Yun, Persistent photoconductivity in Al-doped ZnO photoconductors under air, nitrogen and oxygen ambiance: Role of oxygen vacancies induced DX centers, Ceram. Int. 45 (7) (2019) 8561–8570, https://doi.org/10.1016/j.ceramint.2019.01.174.

[64] Z. Li, W. Wang, N.C. Greenham, C.R. McNeill, Influence of nanoparticle shape on charge transport and recombination in polymer/nanocrystal solar cells, Phys. Chem. Chem. Phys. 16 (47) (2014) 25684–25693, https://doi.org/10.1039/C4CP01111B.

[65] C. Park, S.-M. Lee, W.S. Chang, Carrier transport behaviors depending on the two orthogonally directional energy bands in the ZnO nanofilm affected by oxygen plasma, Phys. Chem. Chem. Phys. 18 (37) (2016) 26184–26191, https://doi.org/10.1039/C6CP04391G.